RESEARCH ARTICLE

Detection of melanin influence on skin samples based on Raman spectroscopy and optical coherence tomography dual-modal approach

Di Wu[1] ⬤ | **Anatoly Fedorov Kukk**[1] ⬤ | **Bernhard Roth**[1,2] ⬤

[1]Hannover Centre for Optical Technologies, Leibniz University Hannover, Hanover, Germany

[2]Cluster of Excellence PhoenixD, Leibniz University Hannover, Hannover, Germany

Correspondence
Di Wu, Hannover Centre for Optical Technologies, Leibniz University Hannover, Nienburger Str. 17, 30167 Hanover, Germany.
Email: di.wu@hot.uni-hannover.de

Abstract

Melanoma is responsible for more than half of the deaths related to skin cancer in the last few decades. A dual-modality optical biopsy system with Raman spectroscopy and optical coherence tomography approach was built with the goal of achieving noninvasive skin measurement. To mimic melanoma and evaluate the effect of melanin on skin,

models have been created by dissolving synthetic melanin in dimethyl sulfoxide and adding it to fresh skin samples. Compared to the untreated samples, morphological images showed that the imaging depth on melanin-treated skin has been increased from 250 μm to 350 μm due to the optical clearing effect of the DMSO solvent, and Raman analysis revealed that relative spectral intensities of melanin-treated samples were lower in the amide-I and CH_2-deformation bands, and higher in the CH_2-twist and C–C stretch bands. Using machine learning for skin type classification, an accuracy of 89% is achieved.
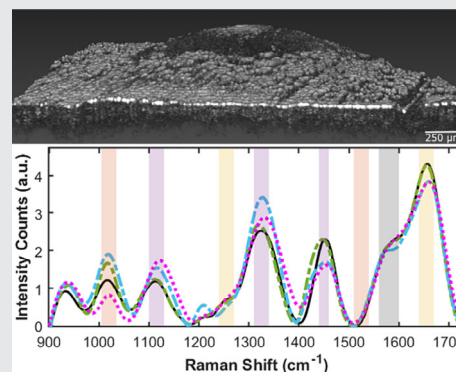
KEYWORDS
dual-modality optical system, melanin in skin, noninvasive melanoma diagnostics, optical coherence tomography, Raman spectroscopy

1 | INTRODUCTION

In recent decades, more than half of skin cancer-related deaths have been attributed to melanoma, and the number of new cases of the latter has been steadily increasing. The American Cancer Society estimates that in 2022, there was a 31% increase in the number of newly diagnosed cases and a 6.5% increase in melanoma mortality [1]. Unfortunately, it is easy to overlook melanoma and misidentify them as birthmarks or moles, delaying the most appropriate time for treatment. In addition, melanoma is prone to metastasis, even in the

asymptomatic stages. Once it spreads to the lymphatic system, the 10-year survival rate is dramatically reduced to 35% [2]. The survival rate is directly related to the melanoma depth. At the early stages (depth <1 mm), the 5-year survival rate is 95%–100%; for late stages (depth >4 mm), the 5-year survival probability drops to under 30% [3].

The initial diagnosis of cutaneous melanoma is generally made by visual inspection. This visual method cannot guarantee complete precision. Sometimes patients are misdiagnosed as false positives (nonmelanoma diagnosed as melanoma), leading to unnecessary excision surgery, or false negatives (melanoma diagnosed as nonmelanoma), which delays treatment. Dermoscopy is a method to obtain enlarged images of lesions prior to diagnosis, which somewhat reduces the probability of misclassification. However, there is a weakness in these diagnostic approaches: they depend on the diagnosing doctor's experience and professional standing.

If the doctor suspects that a skin spot could be melanoma, the suspicious region will be excised and sent for histopathological evaluation. Although histopathology is the gold standard and established standard of care for the diagnosis of atypical pigmented lesions, it is associated with considerable variability in the interrater [4]. In a large study involving 20 pathologists, the overall performance of correctly diagnosing melanoma using the histopathological method reached a sensitivity of 87% [5] and the diagnostic disagreement between dermatopathologists was as high as 38% in more extreme cases [6]. In this context, especially given the rapidly increasing incidence of melanoma, unbiased, trustworthy, precise, and noninvasive auxiliary diagnostic technology is desirable to improve clinical decision-making.

Recent years have seen the application of numerous noninvasive approaches for the detection of the edge of melanoma and differential diagnosis [7], such as high-frequency ultrasound [8], optoacoustics [9], fluorescence spectroscopy [10], Raman spectroscopy [11], confocal microscopy [12], optical coherence tomography (OCT) [13], and reflectance spectroscopy [14]. However, the diagnosis of melanoma or other types of skin cancer based on the above-mentioned technologies is still in the experimental stage, and no mature medical diagnostic equipment has yet been introduced to the market.

Among noninvasive modalities, OCT is most useful for margin and depth detection [15, 16]. As a well-developed optical imaging technology, it can provide images of the morphology of living tissues with micrometer-level resolution, making it a very attractive technology in the medical field [17]. In the area of skin cancer diagnosis, OCT proved to precisely detect the depth of the lesion, and results consistent with histopathology were obtained [18, 19]. Coleman et al.

showed that depth (less than 1 mm) of superficial basal cell carcinoma lesions can be accurately measured using OCT [20]. Hinz et al. showed that the median tumor thickness of 26 melanocytic lesions measured by OCT was 0.31 mm, very close to the median tumor thickness measured by histopathology, which was at 0.25 mm [21].

On the other hand, Raman spectroscopy, as an effective technology to detect biochemical structures, is also being increasingly used in the biomedical field [22]. It can be employed to identify the differences in the chemical properties of the biological tissue in various diseases because the Raman effect is brought on by molecular vibration in the sample that has been exposed to radiation. Therefore, Raman spectroscopy is considered to be a promising technique for identifying different forms of skin cancer and distinguishing between cancerous and benign tumors. For example, Gniadecka et al. acquired near-infrared Fourier transform Raman spectra of normal and diseased skin and used a neural network to determine the importance of each component of the Raman spectrum. The sensitivity and specificity of the melanoma achieved were 85% and 99%, respectively [23]. Schleusener et al. used fiber probe-based Raman spectroscopy to examine 104 patients with lesions suspected to be skin cancer. The accuracy rate for distinguishing malignant melanoma and pigmented nevi was 91% [24]. Yakimov et al. used both fluorescence and Raman microspectroscopy to investigate the distribution of melanin in the epidermis and found the ratio of melanin-related Raman bands at 1380 and 1570 cm^{-1} may be associated with melanin molecular organization [25].

Because of the complementarity of these two techniques, colocalization measurements utilizing combined OCT and Raman modalities have gained attention in recent years. An integrated system for combined Raman spectroscopy—spectral domain OCT was first proposed by Patil et al. and clinically tested against skin cancer and colon cancer [26, 27]. Also, similar integrated systems have been proposed by Evans et al. and Egodage et al., however, the OCT modality in these systems was only used to provide initial morphological features and guide the placement of the Raman acquisition axis [28, 29]. The integrated system of Varkentin et al. demonstrated agreement between OCT images and histopathology with respect to lesion depth [30]. Chen et al. combined space-shifted Raman spectroscopy with OCT to obtain axial Raman spectral information while realizing transverse scanning [31]. Finally, Ashok et al. revealed that combining information from OCT and RS for cancer diagnosis showed considerable improvements in sensitivity and specificity [32]. Using Raman spectroscopy and OCT separately, they obtained a sensitivity of 89% and 78% and a specificity of 77% and 74% for the discrimination of colonic adenocarcinoma from normal colon tissue,

respectively. When combining the information obtained by these two techniques, both the sensitivity and specificity increased to 94% [32]. In addition to the improvement in accuracy, the combination of OCT and Raman can further improve the flexibility of the measurement. It can not only effectively upgrade the inherent Raman point-by-point signal recording to achieve wide-area spectrum detection, but also accurately position the collection point for targeted Raman acquisition to enable the analysis of different regions of interest on the lesion.

In this work, a dual-modality optical biopsy system comprising an OCT and a Raman spectrometer was constructed to combine the morphological images obtained by OCT with the molecular information obtained by Raman spectroscopy. Unlike the previously mentioned Raman-OCT systems which focus on the excitation laser to provide good signal intensity and spectral resolution, the proposed system uses wide-field Raman excitation and locates the acquisition point by the OCT scanning system (as shown in Figure 1B). This approach reduces the energy density of the laser while maintaining resolution to avoid damage to the human body. The effect of melanin (mainly eumelanin) on the skin is worth exploring because melanoma usually develops in melanin-producing cells. Since the action spectrum is similar for both natural and synthetic melanin [33], synthetic melanin powder was dissolved in DMSO as a reliable model for eumelanin.

The increase in the melanin content of the sample was achieved by immersing the sample in the melanin dissolved in DMSO (M-DMSO) or injecting the M-DMSO solution into the epidermis of the sample. OCT B-scan images of samples immersed in solution were found to have a deeper penetration depth with increasing immersion time. While providing the morphological

characterization of the sample, OCT is also used to precisely locate the melanin spots on the sample. The Raman scattering signal from the designated skin surface is then collected by the Raman system. The intensity of the amide-I, CH_2-twist, C–C stretch, and CH_2-deformation bands in the skin Raman spectra was investigated, being the typical Raman bands of proteins and lipids. Using the above characteristic peak intensities as input, the support vector machine (SVM) algorithm achieved an accuracy of 88.9% in distinguishing normal skin from melanin-rich skin. This demonstrates the potential for clinical use of our dual-mode system. In the following stage, in vivo measurements on suspected melanoma patients will be performed in the clinic and the same characteristics can be utilized for machine learning classification to accomplish noninvasive melanoma or other skin cancer diagnosis.

2 | MATERIALS AND METHODS

2.1 | Experimental setup

Figure 1 shows the schematic diagram of the system. OCT measurements are performed by a configurable spectral domain OCT system with a 900 nm center wavelength that includes a base unit (GAN621, Thorlabs) and a scanning system (OCTP-900, Thorlabs). The scanning system was customized by inserting a dichroic mirror (DM, edge wavelength 805 nm, DMLP805R, Thorlabs) between the galvo-mirror and the beam splitter, to which the Raman collection arm is linked. In this way, the OCT and Raman signals are separated after passing through the DM and directed to different collection devices, thus enabling simultaneous OCT-Raman
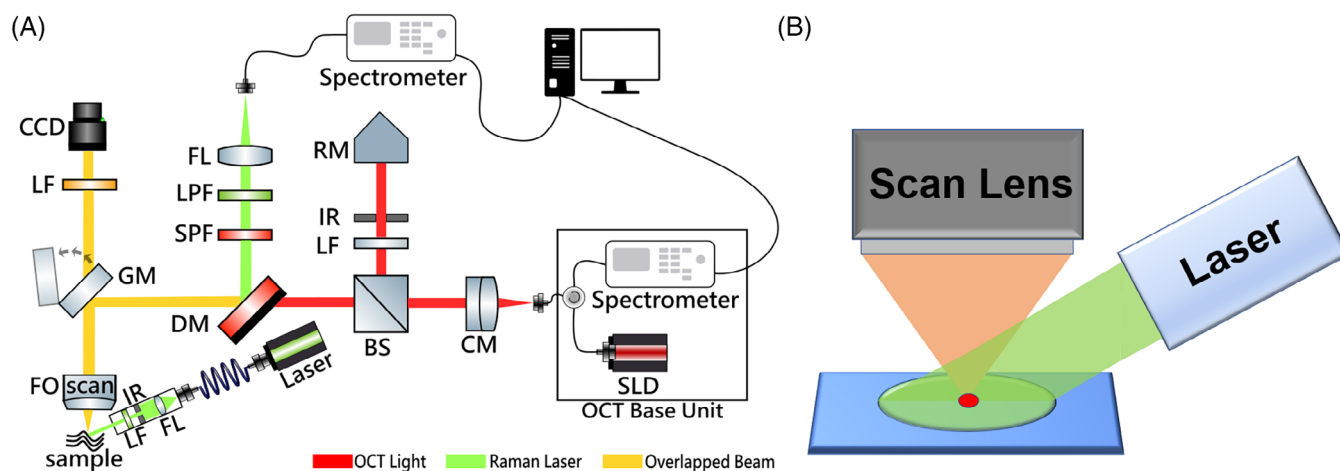

FIGURE 1 (A). Sketch of the experimental setup. BS: beam splitter; CM: collimator; DM: dichroic mirror; FL: focal lens; FO: focal objective lens; GM: galvo mirror; IR: iris; LF: laser filter; LPF: long pass filter; RM: reflector; SL: scan lens; SPF: short pass filter. (B). Sketch of OCT localization: Raman scattering signal is only collected at the focal point of the OCT scanning lens.

measurements. By changing the angle of the galvo mirror, the light emitted from the super luminescence diode with a central wavelength of 900 nm can be focused with a focusing objective (focal length 36 mm, OCT-LK3-BB, Thorlabs) on different positions of the sample. The back-reflected light from the sample and the reflected reference light are detected by a linear CCD array-based spectrometer to generate real-time OCT images.

For the excitation of the Raman scattering signal, a 532 nm pulsed laser (frequency-doubled Nd: YAG laser, 20 Hz repetition rate, 7 ns pulse duration, Ultra50, Quantel Laser, France; the laser energy was kept under the maximum permissible exposure (MPE) standard, as introduced in detail below.) is transmitted through an optical fiber with a core diameter of 910 μm (MPH910L02, Thorlabs) to a self-made collimation head [34], where the laser is collimated by a lens (focal length 40 mm, LB4700, Thorlabs) and irradiated onto the sample with a spot size that can be regulated by an iris. Furthermore, a band-pass filter (with center wavelength 532 nm, bandwidth 4 nm, FLH05532-4, Thorlabs) is integrated at the end of the laser head to filter out the fluorescence and Raman signals generated during transmission in the fiber and the laser head before the laser is directed to the sample.

As with OCT, Raman scattering signals of the sample are collected by the same scanning lens (FO in Figure 1) and then redirected to the Raman collection arm. This ensures that, even when the Raman excitation light is uniformly irradiated over a relatively large skin area to avoid burning the skin, only the Raman scattered signal at the focal point of the scanning lens (approximately 300 μm in diameter) is collected by the spectrometer, allowing the Raman detection to be localized. Before being focused by a focusing lens (focal length 60 mm, AC254-060-A-ML, Thorlabs) and coupled into the fiber bundle (LLB536-IR-0.22-1, Quantum Design GmbH), the Raman signal propagates through a short-pass filter (edge wavelength 700 nm, FESH0700, Thorlabs) and a long-pass filter (edge wavelength 532 nm, RazorEdge ultra-steep LP Edge filter, Semrock Inc.) to ensure thorough filtering of the OCT signal and the Rayleigh scattering signal. The signal is then transferred to a spectrometer (Kymera 193i, Andor Technology Ltd) equipped with a CCD camera (iDus-LDC-DD, Andor Technology Ltd) and a grating (1200 L/mm, 600 nm blaze, Newport Corporation, MKS Instruments, Inc.).

2.2 | Sample preparation

2.2.1 | M-DMSO solution preparation

As a good industrial and biochemical solvent, synthetic melanin is able to be dissolved in dimethyl sulfoxide (DMSO). The polar functional groups in melanin (carboxylic acids and amino acids) can interact with DMSO, while the non-polar groups can form weak hydrophobic interactions with the solvent. In the experiment, 100 mg of synthetic melanin (M8631, Sigma-Aldrich) was dissolved in 100 mL of DMSO (D8418, Sigma-Aldrich) to realize a 1 g/L M-DMSO solution for later use.

2.2.2 | Skin sample preparation

Fresh porcine skin obtained from a local butcher was used to simulate healthy human skin since porcine skin has a very high similarity to human skin in terms of general structure, thickness, pigmentation, protein and lipid composition, and so on [35]. Two methods are implemented to simulate the presence of melanin-rich human skin: one is to infiltrate the porcine skin samples in the M-DMSO solution to simulate a darker skin complexion, and different degrees of dark skin types are simulated by different immersion times; the other is to inject the M-DMSO solution into the epidermis of porcine skin to simulate small areas of melanin deposition on human skin.

Eight sample groups were prepared, each group containing 30–36 porcine skin samples. One group of samples received a needle injection of the M-DMSO solution. For each injection, a needle was used to administer 0.1 mL of 1 g/L M-DMSO solution to the epidermis (approximately 1 mm below the skin surface). Six groups were treated in two ways: three groups were immersed in 1 g/L of M-DMSO solution for 30 min, 1 day, and 2 days, respectively; three control groups were soaked in pure DMSO (D8418, Sigma-Aldrich) for the same time durations. The last group was left untreated.

3 | RESULTS AND DISCUSSION

3.1 | Validation of melanin structures

As a reference, Raman measurements of synthetic melanin powder and the DMSO-dissolved solution were taken. The corresponding Raman spectra are shown in Figure 2. Two distinct broad peaks at 1350 and 1590 cm^{-1} can be seen in the melanin powder spectrum, which is consistent with the measurement results of Huang et al. [36].

However, as a result of fluorescence, the melanin peaks of the M-DMSO solution are difficult to see. In addition, since the efficiency of the diffraction grating reaches its maximum at 600 nm, that is, in the fingerprint region of the Raman spectra obtained from the 532 nm excitation laser, the signal intensity of the original
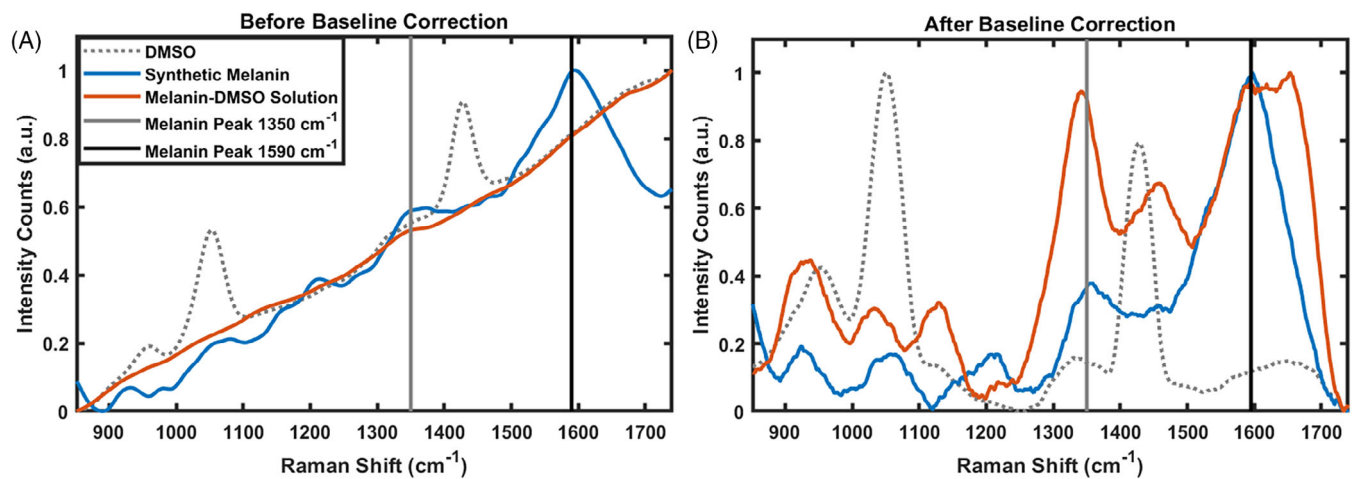
FIGURE 2 Raman spectra of synthetic melanin powder, M-DMSO solution, and DMSO in the range of 800–1800 cm^{-1} (fingerprint region). The spectra are shown before (A) and after (B) baseline correction. Both synthetic melanin and the M-DMSO solution show peaks at 1350 and 1590 cm^{-1}.
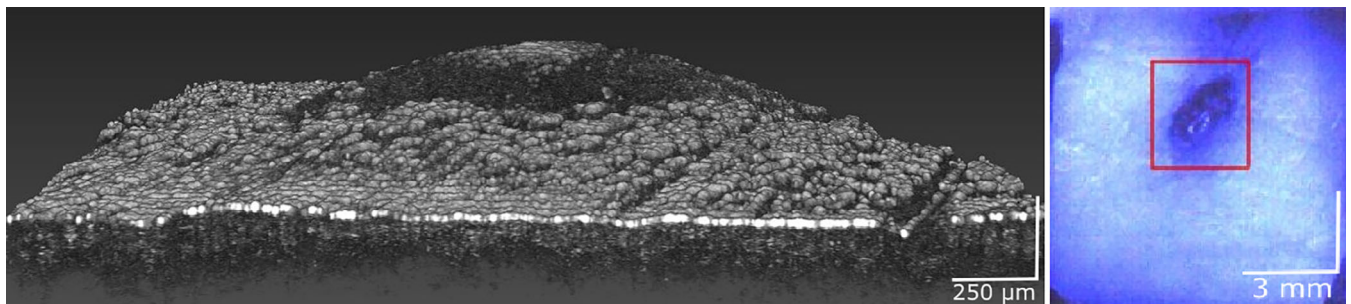

FIGURE 3 The three-dimensional OCT image shows the morphological changes of the samples injected with melanin, and the bulges in the figure are the melanin deposition spots. On the right, an image taken with a CMOS camera located on top of the sample is shown.

spectrum always increases with the increase of the wavenumber. In this case, baseline removal is a very important preprocessing step. The mollifier-based baseline correction method proposed by Koch et al. was used to obtain targeted spectra without interference from background [37]. After the baseline correction, although due to the superposition of fluorescence, some spectral peaks are broadened, the Raman peaks of the M-DMSO solution appeared in the same position as the melanin powder (Figure 2B), which shows that the structure of melanin is preserved after dissolution. In addition, several prominent peaks of DMSO are preserved, for example, at 1050 and 1420 cm^{-1}.

3.2 | OCT morphologic images

Skin samples processed as previously described were subjected to OCT measurements to obtain morphological images. For melanin-injected samples, since the injection was only performed in a small area, OCT is also used to

accurately locate the melanin spots on the samples for subsequent Raman measurements. An example is shown in Figure 3.

In terms of morphology, compared with the untreated skin, the scattering of the sample immersed in the solution is more inhomogeneous, and the imaging depth is larger, which is demonstrated in Figure 4 as more low-intensity pixels appear in the shallow layer (0–300 μm below the skin surface) as well as more high-intensity pixels in the deeper layer (larger than 300 μm).

Considering that DMSO has been shown to reduce the light scattering in skin and that it is widely used in optical tissue clearing [38, 39], one can conclude that DMSO has penetrated the skin, decreased the light scattering in neighboring tissues and increased its transparency. With longer immersion time, more DMSO spreads in the tissue, and less optical scattering occurs. For samples immersed in M-DMSO solution (Figure 4B–D), the contrast is not as obvious as that of the DMSO control groups (Figure 4F–H), mainly because the high light
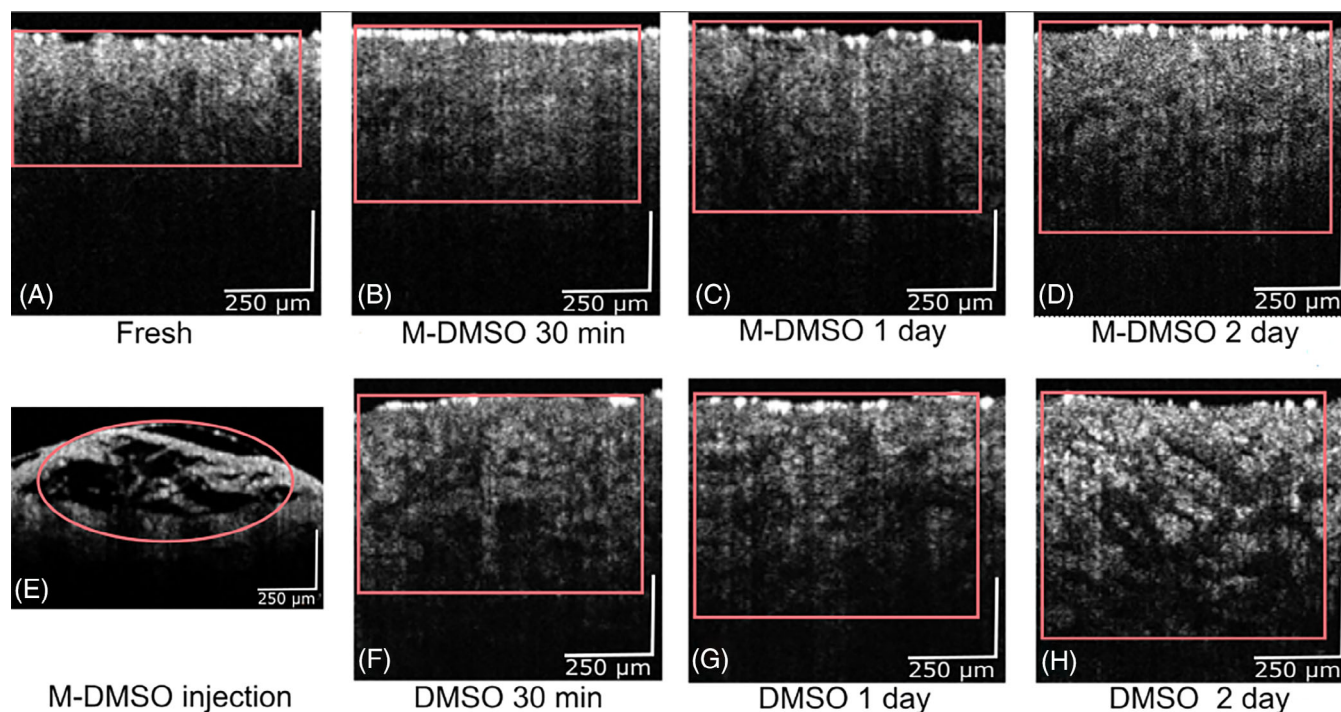
FIGURE 4 Examples of OCT B-scan images of skin for different treatments. (A): fresh skin. (B): skin in M-DMSO solution for 30 min. (C): skin in M-DMSO solution for 1 day. (D): skin in M-DMSO solution for 2 days. (E): skin injected with M-DMSO solution, the black spots in the red circle are the M-DMSO solution left in the epidermis after injection. (F): skin in DMSO for 30 min. (G): skin in DMSO for 1 day. (H): skin in DMSO for 2 days. The red box in the image shows the penetration depth of the OCT signal in skin samples after infiltration with different solutions.

absorption of melanin offsets the optical clearing of DMSO to a certain extent.

To further verify this conclusion, except for the injection group, all OCT A-scan results of each sample (starting from the point with the strongest signal, corresponding to the surface of the skin) were averaged along the B-scan direction. The results are then averaged across all samples in the group to analyze the signal intensity decline along the z-axis of different samples. The results showed that the signal intensity of fresh skin samples decreased more slowly at the beginning and then gradually faster, while at a depth of more than 300 μm, the signal intensity was generally 1–3 dB lower than that of the samples immersed in the solution (Figure 5).

3.3 | Sample spectra

The MPE established by the American National Standards Institute limits the maximum energy to which human skin can be exposed to laser radiation [40]. For single-pulse illumination, the maximum pulse energy E illuminating a certain skin area A should follow the formula:
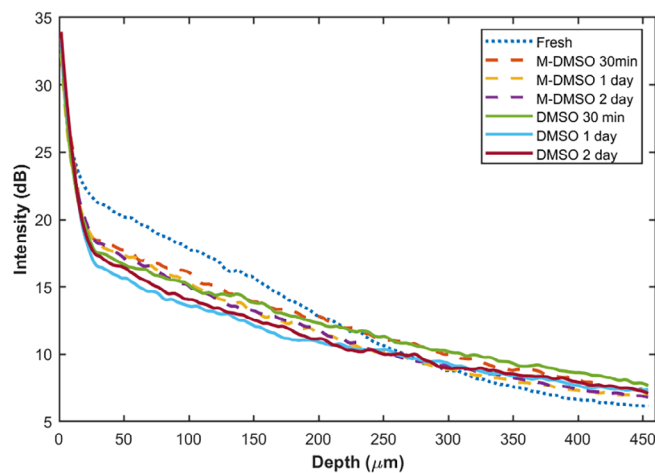

FIGURE 5 Decline of signal intensities of OCT images along the z-axis for different samples.

$$E/A \leq \mathrm{MPE} = 2 \times C_A \times 10^{-2}\,\mathrm{J \cdot cm^{-2}},$$

where C_A is 1.0 for wavelengths between 400 and 700 nm. For the multiple-pulse illumination, besides the irradiance of each pulse during the exposure time t being lower than the MPE for a single pulse, the average

irradiance of the pulse train shall not exceed the MPE for the total pulse train as well, which is found as follows:

$$
\begin{cases}
\dfrac{E \times N \times t}{A} \leq \mathrm{MPE} = 1.1 \times C_A \times t^{0.25} \; \mathrm{J \cdot cm^{-2}}, & t \leq 10 \, \mathrm{s} \\[2mm]
\dfrac{E \times N}{A} \leq \mathrm{MPE} = 0.2 \times C_A \qquad \mathrm{W \cdot cm^{-2}}, & t > 10 \, \mathrm{s}
\end{cases},
$$

where N is the number of pulses in the laser duration. For the above-mentioned laser specification, the calculated skin MPE per single pulse based on different exposure times is illustrated in Figure 6.

In this experiment, even though measurements were performed on ex vivo samples, the irradiation energy is set below the MPE level. This will allow us to compare the findings with the measurements of human skin in the future. Under the current laser specifications (pulse frequency 20 Hz), a 9 x 7 mm^2 area of the sample was investigated, and the average laser energy illuminating the spot is 8 mJ. For every measurement, the exposure time is 5 s. Then, the results of all the samples in the same group were averaged. The obtained Raman spectra are shown in Figure 7. All spectra have nearly identical peak positions, such as the amide-I band at 1650 cm^{-1}, the CH$_2$-twist band at 1320 cm^{-1}, and the ß-carotenoid band at 1005 cm^{-1}.

A notable exception is the spectral peak at 1450 cm^{-1}. Fresh samples, samples immersed in M-DMSO solution for 30 min and 1 day, and samples injected with M-DMSO solution show the peak at this shift, which is the characteristic peak of the CH$_2$-deformation band. However, an additional spectral peak in this region for all samples immersed in DMSO and samples immersed in M-DMSO solution for 2 days appears at around 1427 cm^{-1}, which is the signature for DMSO (see Figure 2). This seems to indicate that the
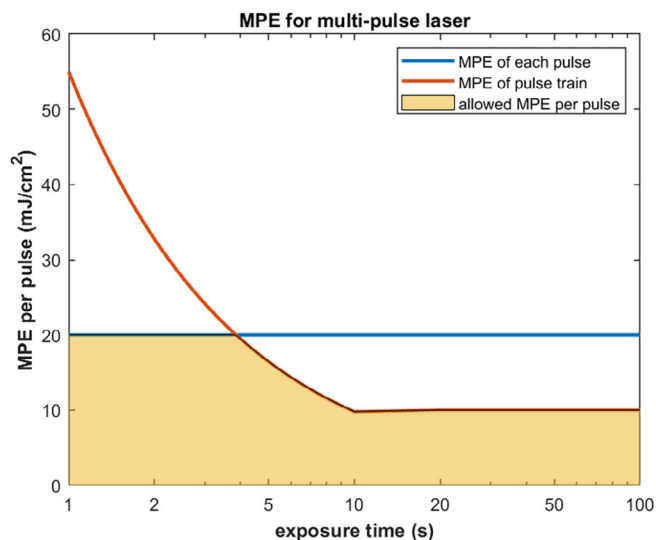
samples are more affected by the solvent when immersed in the M-DMSO solution for too long.

To verify the effect of immersion time on the sample spectra, distinguish the spectra of different samples, and observe the trends, t-distributed stochastic neighbor embedding (t-SNE) was utilized to reduce the dimensionality of the spectral data. t-SNE is a dimensionality reduction technique that is particularly suitable for visualizing high-dimensional datasets and is capable of recovering well-separated groups [41]. The distribution of t-SNE based on the Chebyshev distance metrics is shown in Figure 8. It can be seen that the distribution of the melanin-injected samples is highly concentrated and separates from that of the other skin samples, indicating that altering the melanin content in the epidermis of the sample by injection would have a greater impact on the spectrum of the skin.

In addition, the distribution of spectral data for samples immersed in M-DMSO solution for 30 min is very close to that of fresh skin samples, and when immersed for 1 day, the distribution starts to move away from the distribution of fresh samples. The spectral distribution of the samples immersed for 2 days is mixed with that of the data immersed in DMSO, making it more difficult to distinguish. For the skin immersed in DMSO solution, the distributions are very close for different immersion times, indicating that the effect of DMSO itself on the samples is not very dependent on the immersion time. This result further validates the previous conclusion that the samples are more affected by the DMSO solvent when the immersion time is too long, while the effect of melanin on the sample decreases.

Based on the above findings, the data from samples immersed in M-DMSO solution for 2 days was discarded. The typical lipid and protein peaks in the spectra of all untreated skin samples, samples immersed in M-DMSO solution for 30 min and 1 day, and samples injected with melanin were further analyzed, and the change in relative and absolute peak intensities was determined. As visualized in Table 1 and Figure 9, a long soak in M-DMSO solutions or direct injection of melanin significantly increases the Raman intensity of the samples at 1120 cm^{-1} (C–C stretch) and 1320 cm^{-1} (CH$_2$-twist), while at 1450 cm^{-1} (CH$_2$-deformation) and 1650 cm^{-1} (amide-I, protein), the Raman intensity of the skin treated with the same methods leads to a significant decrease. For short periods of immersion, although the difference is smaller, the same trend is observed.

In the above analysis, the z-score normalization was performed on all spectral data to intuitively compare the intensity of the peaks of the different samples. This however leads to the problem that it is unknown whether the increase in intensity at 1120 and 1320 cm^{-1} is a real
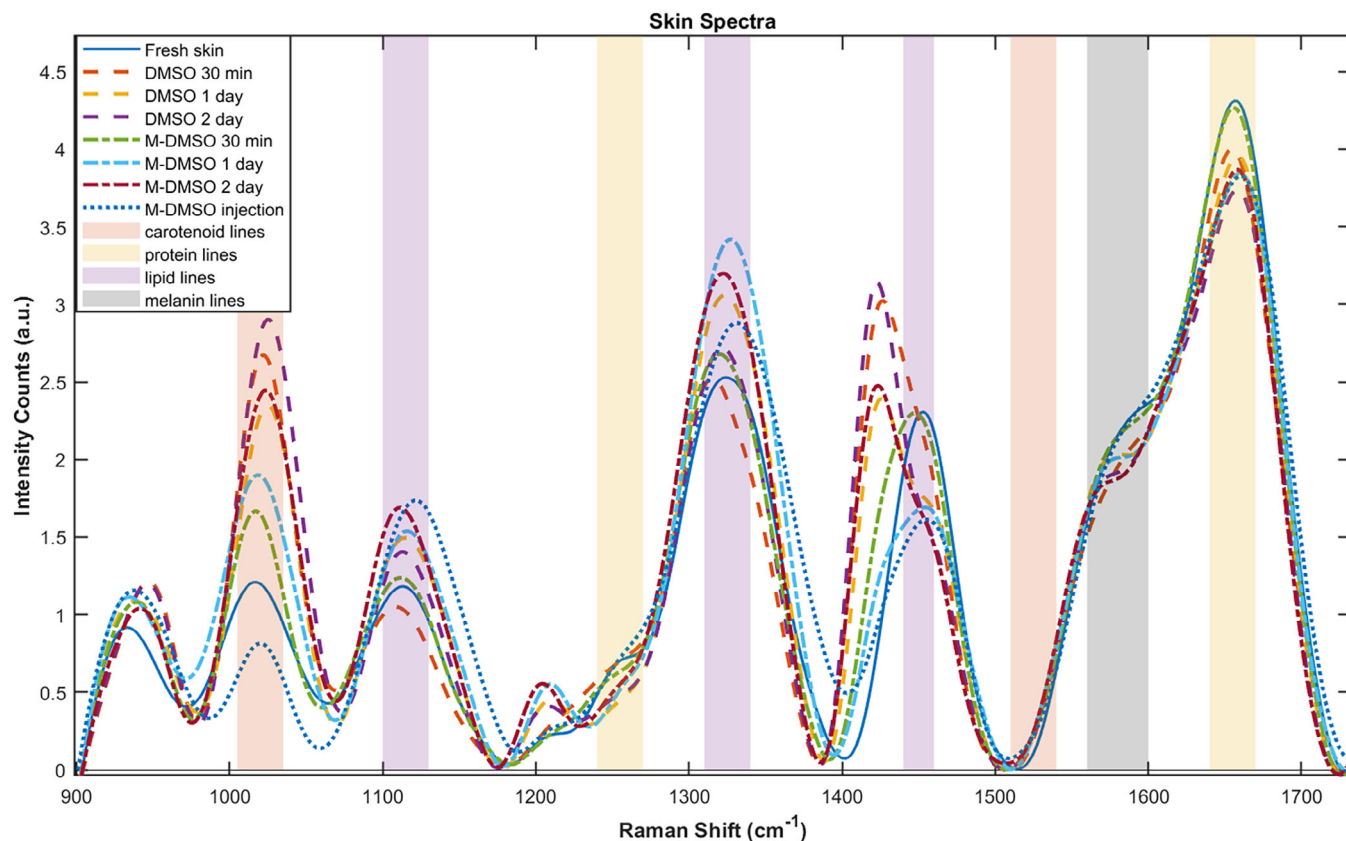
FIGURE 6 The maximum pulse energy allowed to irradiate the skin for a pulsed laser with a repetition rate of 20 Hz.

FIGURE 7 Raman spectra of porcine skin samples under different conditions in the range of 800–1800 cm^{-1}. The peak positions in almost all spectra are comparable.
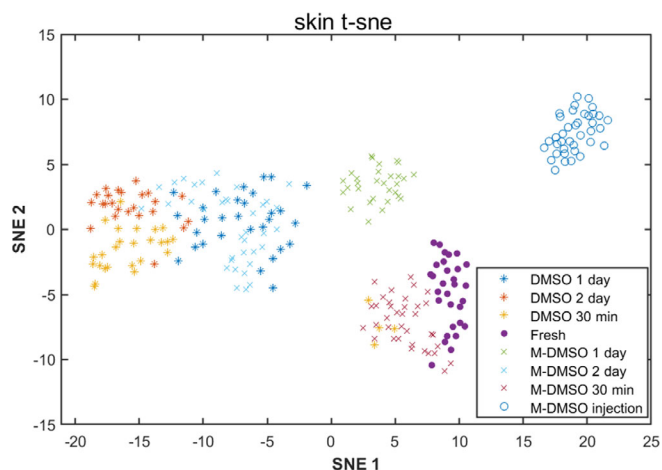

FIGURE 8 The t-SNE distribution of Raman spectral data of porcine skin samples with different treatments. The distribution of Raman spectral data for the samples in DMSO is already noticeably different from that of fresh samples after only 30 min of immersion, whereas the data for samples immersed in M-DMSO solution for the same time are very close to those of fresh samples.

increase or due to a decrease in intensities at other peaks. In this case, the relative intensities of the individual peaks in the spectra were further compared. Taking the intensity of 1650 cm^{-1} as a reference, the relative ratio of

the intensities was calculated. The results are shown in Table 2 and Figure 10.

For short-term immersion, the change is not significant. For long-term immersion and injection, a significant increase is observed in $I_{1120/1650}$ and $I_{1320/1650}$. This is expected because the intensities of the numerators tend to rise, while the denominators tend to fall. Of particular interest is the value of $I_{1450/1650}$, where both the numerator and the denominator had the same downward trend before. This ratio is lower than that of the untreated skin, indicating that melanin has a stronger effect on the CH$_2$-deformation band at 1450 cm^{-1} than on the amide-I band at 1650 cm^{-1}. A possible explanation is that, in the presence of melanin, substances with CH$_2$-deformation structures degrade more than proteins, which leads to a decrease in their content and thus a decrease in the intensity of characteristic Raman peaks.

3.4 | Classification of different skin

To further demonstrate the ability to identify different melanin contents in skin from Raman spectra, an SVM model with Bayesian optimization was constructed.

TABLE 1 Median normalized intensities of typical lipid and protein peaks indifferent melanin-treated skin spectra.

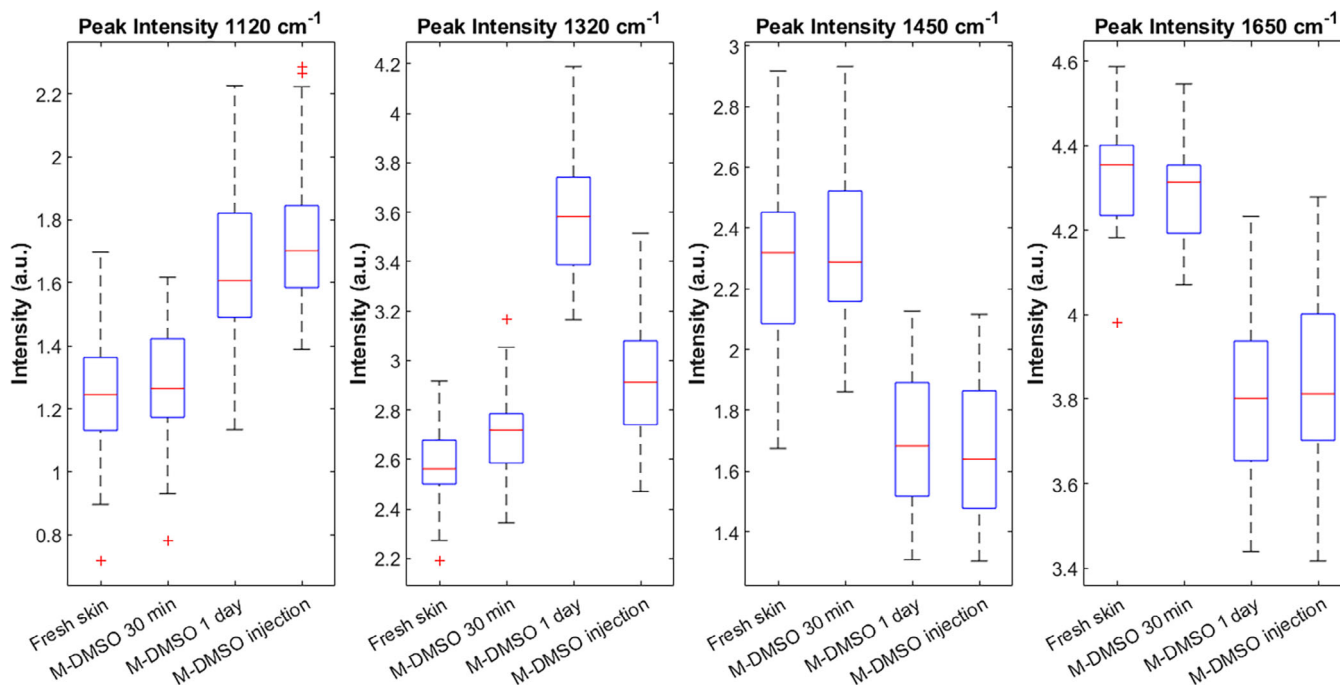| Sample	Position			
	1120 cm^{-1}	1320 cm^{-1}	1450 cm^{-1}	1650 cm^{-1}
Fresh skin	1.24	2.56	2.32	4.35
M-DMSO 30 min	1.26	2.72	2.29	4.31
M-DMSO 1 day	2.23	4.19	1.68	3.80
M-DMSO injection	2.29	2.91	1.64	3.81

FIGURE 9 Intensities of typical lipid and protein peaks in Raman spectra of skin samples with different melanin treatments. Outliers are marked with the red "+."

TABLE 2 Ratio of the median normalized intensities of typical lipid and protein peaks indifferent melanin-treated skin spectra.

Sample	Ratio		
	I$_{1120/1650}$	I$_{1320/1650}$	I$_{1450/1650}$
Fresh skin	0.28	0.60	0.53
M-DMSO 30 min	0.30	0.63	0.53
M-DMSO 1 day	0.43	0.93	0.46
M-DMSO injection	0.46	0.76	0.42

All samples were divided into three categories: samples injected with the M-DMSO solution (M-DMSO injection), samples immersed in the M-DMSO solution (M-DMSO), and untreated samples (Fresh). The absolute and relative intensities of the peaks discussed in the previous section and the carotenoid peak at 1020 cm^{-1} (a significant peak shown in Figure 7) were taken as input parameters. With a 10-fold cross-validation, an accuracy of 88.9% was obtained.

In particular, the confusion matrix in Figure 11 shows that the true positive rate of the two categories of samples with added melanin is 92.2% and 97.1%, respectively, indicating that there is a very high probability of correctly identifying the skin with more melanin content by Raman spectroscopy and demonstrating that the differences in the melanin content of the skin samples are indeed reflected in their Raman spectral information.

3.5 | Discussion

There is a consensus that the melanin content in the epidermis determines the variation in skin color associated with ethnic skin diversity [42]. Another fact is that Caucasian skin types are 5–20 times more likely to develop melanoma than darker skin types [43, 44]. However, exactly how melanin affects melanoma remains controversial.

From the cellular perspective, melanin is widely believed to be involved in cellular degradation and in the activity of
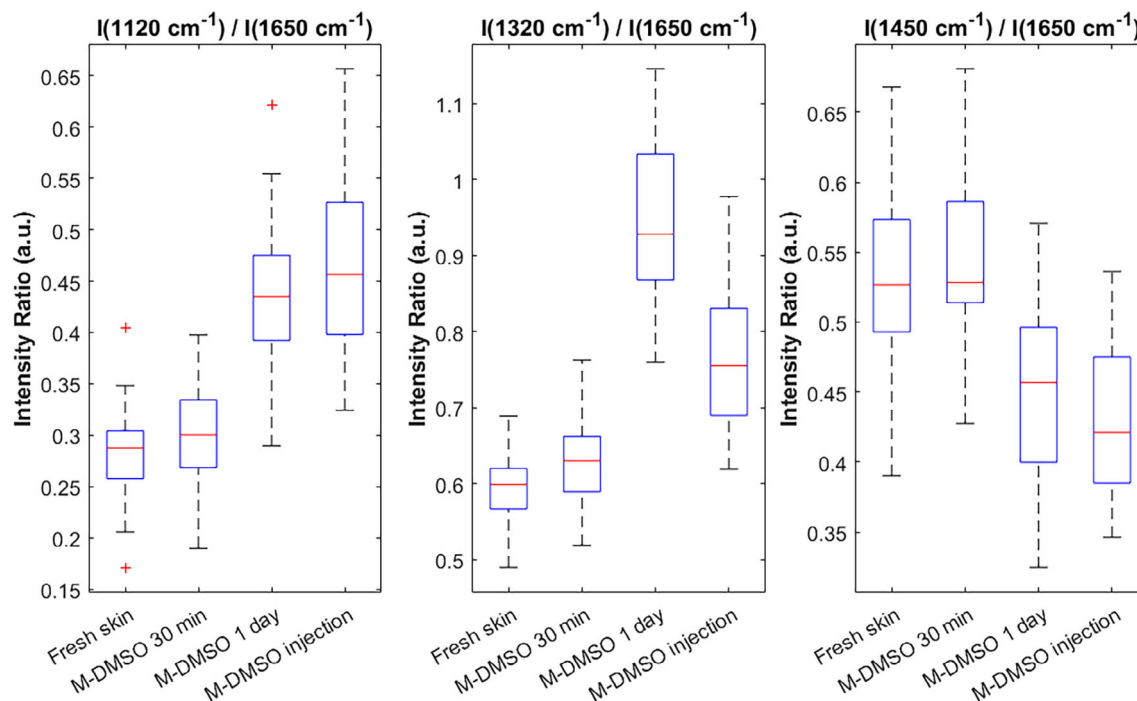
FIGURE 10 Intensity ratios of typical lipid and protein peaks in skin spectra with different melanin treatments (amide-I band at 1650 cm^{-1} as a reference). Outliers are marked with the red "+."

FIGURE 11 The confusion matrix for triple classification using the SVM model, with an accuracy of 88.9%.

certain enzymes. Cell autophagy has been theorized to affect melanosome degradation in keratinocytes [45] and inhibition of autophagy leads to premature aging of melanocytes [46]. The lysosomal degradation process has also been shown to involve melanin granules in the retinal pigment epithelium [47]. In vitro, the melanization of bacteria decreases susceptibility to hydrolytic enzymes of the cell wall [48]. A study shows that synthetic melanin can also inhibit the activity of cytokines [49].

In a study by Huang et al., it was found that in the Raman spectra of hyperpigmented skin, whether it was melanoma, a normal nevus, or just dark skin, a decrease in intensity is obvious at 1450 and 1650 cm^{-1}, compared to the normal skin spectrum [36]. Our study shows that ex vivo skin is also affected by melanin, and when skin samples are immersed in M-DMSO solution or M-DMSO solution is injected, a decrease in intensity is also observed at the same locations (1450 and 1650 cm^{-1}). This may indicate that even if skin cells are dead or deactivated, melanin still affects the breakdown of biomolecules such as proteins and lipids in some way. Furthermore, since the value of I$_{1450/1650}$ in the spectra of melanin-treated samples is lower than that of normal skin samples, we estimate that melanin promotes the degradation of lipids more than proteins.

For the Raman lines at 1320 and 1120 cm^{-1}, considering that these vibrational bands correspond to phospholipids that are the main structures of the cell membrane [50], a reasonable explanation is that melanin does not significantly affect the degradation of membrane-like structures, or perhaps it even promotes their synthesis.

From a histological point of view, the vertical position of atypical melanocytes results in distinct histologic landmarks and cytologic features. Compared with benign nevi, malignant melanoma shows a more disorganized structural order [51], mainly due to its large melanocytes with abundant cytoplasm [52]. Changes in vascular

morphology in malignant melanoma are also a common finding and increase as melanoma becomes more invasive [53].

As an effective morphological diagnostic tool for melanoma, OCT has been found to show certain features of melanoma, such as clear architectural disorganization and blurred dermal-epidermal junction [54]. In addition, some OCT variants such as speckle variance-OCT can identify the microvasculature of the skin [55].

Our study shows that besides the morphological difference, the optical properties are also very noteworthy differences. The difference in the content of melanin in the skin is also reflected in the scattering and absorption of the skin and in the difference in penetration depth on the OCT image.

For the machine learning classification, currently, only the characteristics of the Raman spectra of the samples are considered as input parameters. In the next study, parameters such as OCT signal drop or penetration depth will also be used as input. In this way, the full potential of the suggested OCT-Raman dual-modal system will be exploited, and we believe that it will further improve the accuracy of classification. Also, the ability of these signatures to discriminate melanoma will be further demonstrated by in vivo measurements on melanoma skin cancer patients in a clinical setting.

4 | CONCLUSIONS

A dual-modality RS-OCT optical biopsy system was built to detect the effect of melanin in skin samples. Based on this system, the morphological information and molecular structure information of samples can both be effectively detected within a short time. Melanin was dissolved in DMSO and it was shown that this did not change its structure. Fresh porcine skin samples were immersed in M-DMSO solution or M-DMSO solution was injected into the epidermis of the samples to mimic the effect of darker skin or skin lesions.

The samples were investigated with OCT to study the morphological and optical properties. Melanin-treated skin samples were found to exhibit different scattering and penetration depths for the light. In addition, OCT images were used to localize skin spots containing melanin for subsequent analysis using Raman spectroscopy. A decrease in the intensity of the vibration bands of amide-I and CH_2-deformation was found in melanin-treated skin samples, possibly because melanin promotes the breakdown of biomolecules such as proteins and lipids. After comparing the relative intensities of the two aforementioned vibrational bands, we found that the decrease in the latter was more significant than

the decrease in the former, suggesting that lipids are more affected by melanin than proteins. Using the above characteristic peak intensities as input, the SVM machine learning algorithm achieved 88.9% accuracy in classifying normal and melanin-treated skin in this experiment, which proves that Raman spectroscopy could serve as a basis for the reliable identification of melanoma. Combined with the OCT modality, it could enable the non-invasive detection of skin melanoma in the future.

CONFLICT OF INTEREST STATEMENT
The authors declare no potential conflict of interest.

DATA AVAILABILITY STATEMENT
The data that support the findings of this study are available from the corresponding author upon reasonable request.

ORCID
Di Wu https://orcid.org/0000-0001-5919-7010
Anatoly Fedorov Kukk https://orcid.org/0000-0003-2233-4960
Bernhard Roth https://orcid.org/0000-0001-9389-7125

REFERENCE
[1] R. L. Siegel, K. D. Miller, H. E. Fuchs, A. Jemal, *CA Cancer J Clin* **2021**, *71*, 7.
[2] R. R. White, W. E. Stanley, J. L. Johnson, D. S. Tyler, H. F. Seigler, *Ann. Surg.* **2002**, *235*, 879.
[3] T. Wang, J. Qiu, T. E. Milner, *Determination of Melanoma Lateral and Depth Margins: Potential for Treatment Planning and Five-Year Survival Rate*, IntechOpen, London **2011**.
[4] P. Gerami, Z. Yao, D. Polsky, B. Jansen, K. Busam, J. Ho, M. Martini, L. K. Ferris, *J. Am. Acad. Dermatol.* **2017**, *76*, 114.
[5] L. Brochez, E. Verhaeghe, E. Grosshans, E. Haneke, G. Piérard, D. Ruiter, J.-M. Naeyaert, *J. Pathol.* **2002**, *196*, 459.
[6] E. R. Farmer, R. Gonin, M. P. Hanna, *Hum. Pathol.* **1996**, *27*, 528.
[7] A. M. Glazer, D. S. Rigel, R. R. Winkelmann, A. S. Farberg, *Dermatol. Clin.* **2017**, *35*, 409.

[8] L. Machet, V. Belot, M. Naouri, M. Boka, Y. Mourtada, B. Giraudeau, B. Laure, A. Perrinaud, M. C. Machet, L. Vaillant, *Ultrasound Med. Biol.* **2009**, *35*, 1411.

[9] A. F. Kukk, E. Blumenröther, B. Roth, *Biomed. Phys. Eng. Express* **2022**, *8*, 035029.

[10] M. Panjehpour, C. E. Julius, M. N. Phan, T. Vo-Dinh, S. Overholt, *Lasers Surg. Med.* **2002**, *31*, 367.

[11] H. Lui, J. Zhao, D. McLean, H. Zeng, *Cancer Res.* **2012**, *72*, 2491.

[12] A. Waddell, P. Star, P. Guitera, *Melanoma Manag.* **2018**, *5*, MMT04.

[13] A. Rajabi-Estarabadi, J. M. Bittar, C. Zheng, V. Nascimento, I. Camacho, L. G. Feun, M. Nasiriavanaki, M. Kunz, K. Nouri, *Lasers Med. Sci.* **2019**, *34*, 411.

[14] B. W. Murphy, R. J. Webster, B. A. Turlach, C. J. Quirk, C. D. Clay, P. J. Heenan, D. D. Sampson, *J. Biomed. Opt.* **2005**, *10*, 064020.

[15] A. F. Kukk, D. Wu, E. Gaffal, R. Panzer, S. Emmert, B. Roth, *J. Biophoton.* **2022**, *15*, e202200129.

[16] A. Varkentin, M. Mazurenka, E. Blumenröther, M. Meinhardt-Wollweber, M. Rahlves, S. M. C. Broekaert, S. Schäd-Trcka, S. Emmert, U. Morgner, B. Roth, *J. Biophoton.* **2017**, *10*, 854.

[17] A. Varkentin, M. Otte, M. Meinhardt-Wollweber, M. Rahlves, M. Mazurenka, U. Morgner, B. Roth, *J. Opt.* **2016**, *18*, 125302.

[18] A. Rajabi-Estarabadi, J. M. Bittar, C. Zheng, V. Nascimento, I. Camacho, L. G. Feun, M. Nasiriavanaki, M. Kunz, K. Nouri, *Lasers Med. Sci.* **2019**, *34*, 411.

[19] J. Welzel, E. Lankenau, R. Birngruber, R. Engelhardt, *J. Am. Acad. Dermatol.* **1997**, *37*, 958.

[20] A. J. Coleman, T. J. Richardson, G. Orchard, A. Uddin, M. J. Choi, K. E. Lacy, *Skin Res. Technol.* **2013**, *19*, e10.

[21] T. Hinz, L.-K. Ehler, H. Voth, I. Fortmeier, T. Hoeller, T. Hornung, M.-H. Schmid-Wendtner, *Dermatology* **2011**, *223*, 161.

[22] K. A. Antonio, Z. D. Schultz, *Anal. Chem.* **2014**, *86*, 30.

[23] M. Gniadecka, P. A. Philipsen, S. Wessel, R. Gniadecki, H. C. Wulf, S. Sigurdsson, O. F. Nielsen, D. H. Christensen, J. Hercogova, K. Rossen, H. K. Thomsen, L. K. Hansen, *J. Invest. Dermatol.* **2004**, *122*, 443.

[24] J. Schleusener, P. Gluszczynska, C. Reble, I. Gersonde, J. Helfmann, J. W. Fluhr, M. C. Meinke, *Exp Dermatol* **2015**, *24*, 767.

[25] B. P. Yakimov, E. A. Shirshin, J. Schleusener, A. S. Allenova, V. V. Fadeev, M. E. Darvin, *Sci. Rep.* **2020**, *10*, 1.

[26] C. A. Patil, N. Bosschaart, M. D. Keller, T. G. van Leeuwen, A. Mahadevan-Jansen, *Opt. Lett.* **2008**, *33*, 1135.

[27] C. A. Patil, H. Kirshnamoorthi, D. L. Ellis, T. G. van Leeuwen, A. Mahadevan-Jansen, *Lasers Surg. Med.* **2011**, *43*, 143.

[28] J. W. Evans, R. J. Zawadzki, R. Liu, J. W. Chan, S. M. Lane, J. S. Werner, *J. Biophoton.* **2009**, *2*, 398.

[29] K. D. Egodage, S. Dochow, T. Bocklitz, O. Chernavskaia, C. Matthäus, M. Schmitt, J. Popp, *J. Biomed. Photon. Eng.* **2015**, *1*, 169.

[30] A. Varkentin, M. Mazurenka, E. Blumenröther, L. Behrendt, S. Emmert, U. Morgner, M. Meinhardt-Wollweber, M. Rahlves, B. Roth, *J Biophoton.* **2018**, *11*, e201700288.

[31] M. Chen, J. Mas, L. H. Forbes, M. R. Andrews, K. Dholakia, *J. Biophoton.* **2018**, *11*, e201700129.

[32] P. C. Ashok, B. B. Praveen, N. Bellini, A. Riches, K. Dholakia, C. S. Herrington, *Biomed. Opt. Express* **2013**, *4*, 2179.

[33] T. Sarna, R. C. Sealy, *Photochem. Photobiol.* **1984**, *39*, 69.

[34] M. Mazurenka, L. Behrendt, M. Meinhardt-Wollweber, U. Morgner, B. Roth, *Rev. Sci. Instrum.* **2017**, *88*, 105103.

[35] A. Summerfield, F. Meurens, M. E. Ricklin, *Mol. Immunol.* **2015**, *66*, 14.

[36] Z. Huang, H. Lui, M. X. K. Chen, A. Alajlan, D. I. McLean, H. Zeng, *J. Biomed. Optmn.* **2004**, *9*, 1198.

[37] M. Koch, C. Suhr, B. Roth, M. Meinhardt-Wollweber, *J. Raman Spectrosc.* **2017**, *48*, 336.

[38] A. K. Bui, R. A. McClure, J. Chang, C. Stoianovici, J. Hirshburg, A. T. Yeh, B. Choi, *Lasers in Surgery and Medicine: The Official Journal of the American Society for Laser Medicine and Surgery* **2009**, *41*, 142.

[39] E. A. Genina, A. N. Bashkatov, E. A. Kolesnikova, M. V. Basko, G. S. Terentyuk, V. V. Tuchin, *J. Biomed. Opt.* **2014**, *19*, 021109.

[40] ANSI Z136.1 Laser Safety Standard for the Safe Use of Lasers. Technical report, Laser Institute of America. **2014**.

[41] G. C. Linderman, S. Steinerberger, *SIAM J. Math. Data Sci.* **2019**, *1*, 313.

[42] W. C. Quevedo Jr., T. J. Holstein, *The Pigmentary System: Physiology and Pathophysiology*, John Wiley & Sons, Hoboken, New Jersey **2006**, p. 61.

[43] A. N. Houghton, D. Polsky, *Cancer Cell* **2002**, *2*, 275.

[44] M. M. Clairwood, J. Ricketts, J. Grant-Kels, L. Gonsalves, *Int. J. Dermatoly* **2014**, *53*, 425.

[45] D. Murase, A. Hachiya, K. Takano, R. Hicks, M. O. Visscher, T. Kitahara, T. Hase, Y. Takema, T. Yoshimori, *J. Invest. Dermatol.* **2013**, *133*, 2416.

[46] C.-F. Zhang, F. Gruber, C. Ni, M. Mildner, U. Koenig, S. Karner, C. Barresi, H. Rossiter, M.-S. Narzt, I. M. Nagelreiter, L. Larue, D. J. Tobin, L. Eckhart, E. Tschachler, *J. Invest. Dermatol.* **2015**, *135*, 1348.

[47] U. Schraermeyer et al., *Exp. Eye Res.* **1999**, *68*, 237.

[48] Á. L. Rosas, A. Casadevall, *Mycopathologia* **2001**, *151*, 53.

[49] N. Mohagheghpour, N. Waleh, S. J. Garger, L. Dousman, L. K. Grill, D. Tusé, *Cell. Immunol.* **2000**, *199*, 25.

[50] P. R. Carey, *Biochemical Applications of Raman and Resonance Raman Spectroscopes*, Vol. 8, Elsevier, Amsterdam, Netherlands **1982**, p. 212.

[51] A. G. Goodson, D. Grossman, *J. Am. Acad. Dermatol.* **2009**, *60*, 719.

[52] T. D. Menge, G. Pellacani, *Semin Cutan Med Surg* **2016**, *35*, 18.

[53] S. Schuh, J. Holmes, M. Ulrich, L. Themstrup, G. B. E. Jemec, N. de Carvalho, G. Pellacani, J. Welzel, *Dermatolo The* **2017**, *7*, 187.

[54] M. Mogensen, L. Thrane, T. M. Jørgensen, P. E. Andersen, G. B. E. Jemec, *J. Biophoto.* **2009**, *2*, 442.

[55] J. Olsen, L. Themstrup, G. B. Jemec, *G. Ital. Dermatol. Venereol.* **2015**, *150*, 603.